[20]This method was used several years ago to derive the equations of Ref. 1. More recently the methods of Kadanoff and Baym have been invoked in an attempt to derive the relaxation rates to infinite order in J: (a) W. Brenig, W. Gotze, and P. Wölfle, Phys. Letters 30A, 448 (1969); (b) P. Wölfle, W. Brenig, and W. Gotze, Z. Physik 235, 59 (1970); (c) W. Brenig, W. Gotze, and P. Wölfle, Phys. Rev. B 2, 4533 (1970); (d) P. Wölfle (unpublished). Unfortunately these authors do not give the details of their derivation. Their equations do not contain torque terms and hence cannot be used to describe spin resonance even to zeroth order in J, although they add them, apparently phenomenologically later. Secondly, although purporting to deal with the Kondo effect, they completely miss the leading order Kondo logarithmic term. We therefore will not discuss this work further.

[21]We find this technique more convenient in the present calculations than the pseudofermion representation of A. A. Abrikosov, Physics 2, 5 (1965). This technique was apparently first used independently by P. A. Fedders (Ref. 18) and about the same time by us in the derivation announced in Ref. 1. It was later used by Brenig and Götze [Z. Physik 217, 188 (1968)] and again in Ref. 20.

[22]D. C. Langreth and J. W. Wilkins, Phys. Rev. (to be published).

[23]Henceforth in this paper we choose units such that $\hbar = 1$.

[24]It has just been pointed out to us that a similar notation was used by V. Keldysh, Zh. Eksperim. i Teor. Fiz. 47, 1515 (1964) [Sov. Phys. JETP 20, 1018 (1965)]. In fact one form of the generalized Kadanoff-Baym equations is given there. Very recently, equations similar to those used here and in Ref. 1 have been applied to the interacting Fermi Liquid [P. Wölfle, Z. Physik 232, 38 (1970)].

[25]See the Appendix in Ref. 19. A few distinctions and clarifications are in order. First, we are calculating the self-energy and not the Green's function, and hence the initial and final Green's functions are omitted along with two time integrals. Second, the vertices are ordered in the way they appear in Fig. 1 in which the earlier time is on the right (while the reverse is true in Ref. 19). Lines entering (leaving) a vertex multiply it on the right (left).

PHYSICAL REVIEW B VOLUME 6, NUMBER 9 1 NOVEMBER 1972

Correlated Electron Paramagnetic Resonance and Optical Study of $CdF_2:Er^{3+}$. I. C_{2v} Local-Site Symmetry

T. C. Ensign and N. E. Byer
Research Institute for Advanced Studies,
Martin Marietta Corporation, 1450 *South Rolling Road, Baltimore, Maryland* 21227
(Received 10 April 1972)

A correlated EPR and optical study has been performed on CdF_2: (Er^{3+}, U) ($U \equiv$ unintentionally compensated) and CdF_2: (Er^{3+}, M^+) ($M^+ = Li^+$, Na^+, Ag^+, or K^+) crystals with the following objectives: (i) generating a high concentration of a specific (i.e., C_{2v}) Er^{3+} site through the addition of monovalent cations and characterizing this site by EPR; (ii) unambiguously determining selected optical properties of Er^{3+} in C_{2v} symmetry; and (iii) determining the crystal field splitting of the $^4I_{15/2}$ ground site of Er^{3+} for C_{2v} symmetry. The orthorhombic (C_{2v}) symmetry, produced at the erbium site when M^+ ions are introduced for charge compensation, has been identified through the angular dependence of the Er^{3+} EPR spectrum (at 4.2 K). Moreover, the EPR results reveal that the C_{2v} (Er^{3+}, M^+) site accounts for nearly all (> 98%) of the noncubic sites recorded for (Er^{3+}, M^+) specimens. This result has permitted an unambiguous determination of the emission, excitation, absorption, lifetime, and efficiency properties of Er^{3+} in C_{2v} symmetry. These characteristics have been found to be similar for each of the M^+ ions listed, but different from those obtained from (Er^{3+}, U) crystals. In particular for (Er^{3+}, Na^+) the green ($^4S_{3/2} \rightarrow {}^4I_{15/2}$) quantum yield is observed to increase from 2.3 to 19.7%, whereas the red ($^4F_{9/2} \rightarrow {}^4I_{15/2}$) quantum yield decreases from 26 to 2.9%. The large variation in these radiative-quantum yields is analyzed in terms of multiphonon decay processes ($^4S_{3/2} \rightarrow {}^4F_{9/2}$), which are seen to be sensitive to Er^{3+}-site symmetry, but relatively insensitive to the exact nature of the compensating species. The crystal field splitting of the $^4I_{15/2}$ ground state of Er^{3+} in C_{2v} symmetry is in good agreement with that expected from the cubic-field approximation of Lea, Leask, and Wolf, with crystal field parameters, $A_4\langle r^4\rangle = -245$ cm^{-1} and $A_6\langle r^6\rangle = 40$ cm^{-1}. The noncubic portion of the total orthorhombic field may be accounted for in terms of an axial distortion along the $Er^{3+}-M^+$ direction, as verified by the excellent agreement obtained between the EPR g values and the optical splitting of the $\Gamma_8^{(1)}$ state of the $^4I_{15/2}$ multiplet.

I. INTRODUCTION

The optical spectra of Er^{3+} in crystals exhibiting the fluorite structure, space group O_h^5 ($Fm3m$), very often exhibit complex structure. Electron-paramagnetic-resonance (EPR) studies of these crystals have shown that this structure arises because the Er^{3+} may reside in a variety of noncubic

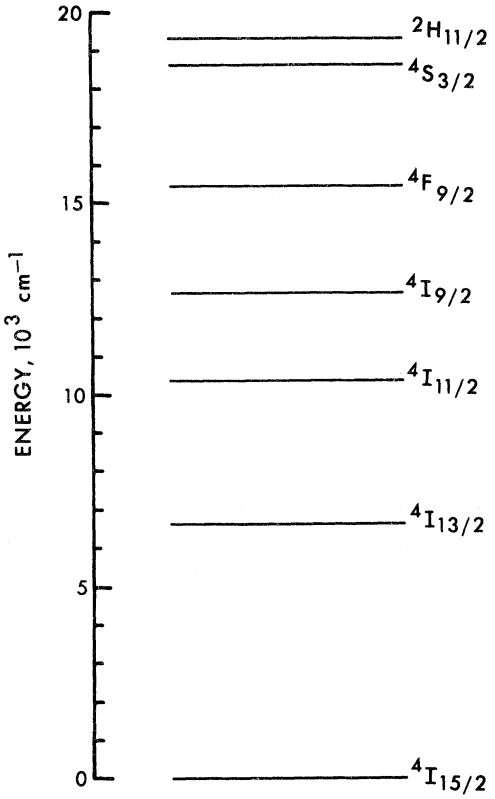

FIG. 1. Energy-level diagram for Er^{3+} in CdF_2. Optical-absorption data have been used to determine the separations between the bottoms of the Er^{3+} multiplets, as depicted.

sites. For example, several tetragonal[1-6] and trigonal[3-5,7,8] Er^{3+} sites have been identified in the alkaline earth fluorides CaF_2, SrF_2, and BaF_2. CdF_2 also exhibits the fluorite structure, and recently our EPR measurements[9-11] have identified the first noncubic-Er^{3+} sites (i.e., trigonal[9,10] and orthorhombic[11]) reported for this material.

The superposition of optical spectra corresponding to ions in various lattice sites[12,13] and the absence of many expected spectral lines[14] make it difficult to assign a set of optical transitions to a particular site.[15,16] Chemical and thermal techniques for treating fluorite crystals (e.g., oxygen firing[17] and monovalent-ion doping[18]) have been employed with varying degrees of success to influence the manner in which the excess charge of the Er^{3+} is compensated and thereby to generate selectively a specific Er^{3+} site. Unfortunately, crystals modified in this way have rarely been subjected to analyses sufficiently detailed to permit identifying the optically active ion sites.

This paper describes a coordinated study of EPR and optical characteristics of Er^{3+} in orthorhombic symmetry.[11] Primary emphasis is given to those properties associated with the $^2H_{11/2}$, $^4S_{3/2}$, $^4F_{9/2}$ and $^4I_{15/2}$ multiplets of Er^{3+}, depicted in Fig. 1. The principal crystals investigated were CdF_2: (Er^{3+}, M^+) ($M^+ = Li^+$, Na^+, Ag^+, or K^+), for which the relevant properties are outlined in Sec. II. Experimental procedures are described in Sec. III. The orthorhombic (C_{2v}) symmetry and the relative distribution of Er^{3+} sites arising from M^+ charge compensation are determined by EPR in Sec. IV A, together with a characterization of these sites for different M^+ ions. Optical spectra unambiguously correlated with orthorhombic-Er^{3+} sites are reported for the first time in Sec. IV B. The crystal field splitting of the $^4I_{15/2}$ ground state was determined experimentally (Sec. IV C) and found to be in good agreement with the cubic-crystal-field approximation using the formalism of Lea, Leask, and Wolf[19] outlined in Sec. V A. Perturbations due to the noncubic components of the crystal field are also discussed in Sec. V A. In Sec. V B, the effect of multiphonon-decay processes on the radiative quantum yields are discussed, and the multiphonon rates are shown to depend upon the crystalline environment of the Er^{3+} ion.

II. CRYSTAL PROPERTIES

In the fluorite lattice structure exhibited by CdF_2, each cadmium ion is surrounded by eight fluorine ions, giving rise to the O_h symmetry shown in Fig. 2(a). The substitution of trivalent-

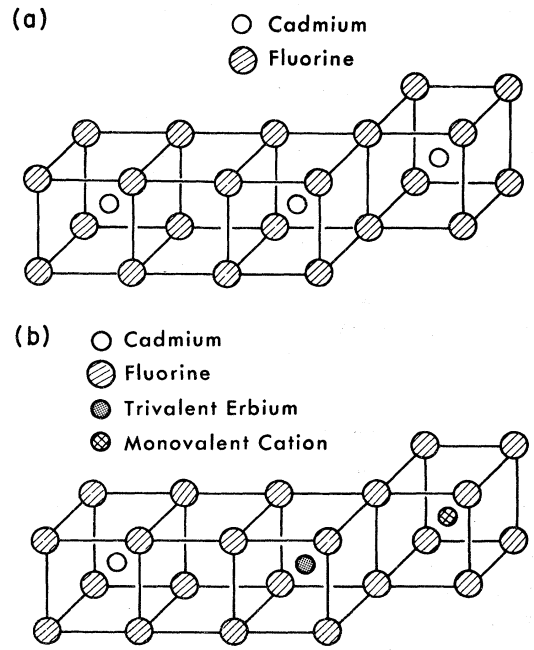

FIG. 2. Fluorite crystal structure of CdF_2: (a) in the pure state; (b) showing a trivalent erbium ion substituting for Cd^{2+} with charge compensation provided by a monovalent cation M^+ located along a ⟨110⟩ crystal direction.

erbium ions for the divalent-cadmium ions implies the necessity for charge compensation which may be achieved in various ways. In particular, the orthorhombic (C_{2v}) point symmetry illustrated in Fig. 2(b) results if charge compensation is effected by substituting a monovalent cation M^+ for one of the Cd^{2+} ions nearest to the Er^{3+}. This paper is concerned with the characteristics of Er^{3+} in sites of C_{2v} symmetry produced when different monovalent cations ($M^+ = Li^+$, Na^+, Ag^+, or K^+) provide the change compensation.

The single crystals of CdF_2 investigated in this study were grown in a "dynamic" vacuum (2.5×10^{-2} Torr) by the Bridgman–Stockbarger technique using high-purity CdF_2 starting material to which were added 0.1-mole% ErF_3 and 1.0-mole% MF.[20] EPR measurements indicated, however, that substantial fractions of the M^+ ions were lost by vaporization and segregation effects during crystal growth.[21] Crystals containing no intentionally added monovalent cations, but prepared otherwise in the same manner as the double-doped specimens, were studied also. In the remainder of this paper, these crystals are referred to as $CdF_2:(Er^{3+}, U)$.

III. EXPERIMENTAL

A. Electron-Paramagnetic-Resonance Studies

The EPR spectra of $CdF_2:(Er^{3+}, M^+)$ and $CdF_2:(Er^{3+}, U)$ have been investigated using specimens in which a $\{110\}$ crystalline plane had been located by the technique of Laue back reflection. Oriented samples of CdF_2 (approximately $1\times3\times7$ mm) were cut from the boule, and the same samples (or closely similar ones) were used in both the EPR and the optical studies. The EPR spectra of Er^{3+} were recorded at 4.2 K using a modified Varian model No. V4502 X-band spectrometer (operating in the low-power mode) and a 12-in. rotating electromagnet. Spectra were obtained as a function of magnetic-field orientation and were calibrated using a Varian model No. F-8 fluxmeter, a Hewlett Packard model No. 5246L electronic counter, and a Hewlett Packard model No. 5255A frequency converter.

B. Photoluminescence Studies

Photoluminescence measurements were made by exciting the CdF_2 samples with a monochromatic source (i.e., a 500-W xenon-arc lamp and a $\frac{1}{4}$-m Spex monochromator) and sensing the fluorescence perpendicular to the direction of excitation. Detection of the emitted light was accomplished using a $\frac{3}{4}$-m Spex grating monochromator, a RCA 7265 photomultiplier (S20 response), and a PAR model No. HR-8 lock-in amplifier that was synchronized with a light chopper in the excitation beam. Emission spectra were recorded in terms of emitted power vs wavelength, with the excitation wavelength fixed. Excitation spectra were obtained such that the emitted power was a function of the excitation wavelength, with the wavelength of the detector bandpass fixed. Low-temperature photoluminescence spectra were obtained using an immersion Dewar (at 4.2 and 77 K).

C. Optical-Lifetime Studies

The phase-lag method[22] was employed to determine the lifetime τ from the relation

$$\tau = \tan\phi / 2\pi f , \tag{1}$$

where f is the chopper modulation frequency and ϕ is the phase shift (analyzed by the lock-in amplifier) between the excitation and the emission for the first Fourier component. Equation (1) is valid when the decay is characterized by a single time constant, which was verified experimentally by comparing τ at various modulation frequencies.

D. Radiative Quantum Efficiencies

The photoluminescence apparatus was used also in the determination of radiative efficiencies. In order to insure accuracy and reproducibility, it was necessary to mount the CdF_2 specimens in a well-defined geometry. A mask with rectangular excitation and emission apertures was used for this purpose. The power $P(\nu_i)$ transmitted through the excitation aperture with frequency ν_i was measured with an Eppley silver-bismuth thermopile. In order to determine the spectral responsivity $R(\nu_0)$ of the detection system to radiation with frequency ν_0, the response of this system to the emission from a diffuse monochromatic source was recorded. The monochromatic source consisted of opal glass illuminated by the excitation source and mounted in place of the sample. For this purpose, $R(\nu_0)$ is defined in terms of the radiance of the diffuse source $N(\nu_0)$, where

$$R(\nu_0) = i(\nu_0)/N(\nu_0) \tag{2}$$

and $i(\nu_0)$ is the anode current of the phototube. $N(\nu_0)$ was obtained using a silicon solar cell calibrated against the Eppley thermopile.

The quantum efficiency $Q(\Gamma_i, \Gamma_0)$ relates the number of photons per second $\Delta N(\Gamma_0)$ emitted in a band Γ_0 to the number of photons absorbed per second $\Delta N(\Gamma_i)$ in the band Γ_i, that is,

$$Q(\Gamma_i, \Gamma_0) = \Delta N(\Gamma_0)/\Delta N(\Gamma_i) , \tag{3}$$

where the bands Γ_i, Γ_0 correspond to the transitions between the various multiplets of the optically active ion. The geometry of the experimental setup defines a volume $V_L = w_i w_0 l$, where $w_i(w_0)$ is the excitation (emission) aperture width and l is the height (the same for both apertures). This

volume is the luminescing region of the sample that is sensed by the detector. The number of quanta absorbed per second in V_L is

$$\Delta N(\Gamma_i) = T[P(\nu_i)/h\nu_i] \int_{\Gamma_i} G(\nu-\nu_i) w_0 \alpha(\nu) d\nu , \quad (4)$$

where T is the transmissivity of the sample-to-air interface, $\alpha(\nu)$ is the absorption coefficient, and the integral is over the absorption band Γ_i. The line-shape function of the excitation source $G(\nu-\nu_i)$ with center frequency ν_i is normalized as follows:

$$\int_0^\infty G(\nu-\nu_i) d\nu = 1 , \quad (5)$$

where the half-width of $G(\nu-\nu_i)$ is small compared to ν_i. The assumption was made that $w_0\alpha(\nu) \ll 1$, which is valid for this study ($w_0 = 0.5$ cm, $\alpha < 0.2$ cm^{-1}). The number of quanta emitted per second from V_L is

$$\Delta N(\Gamma_0) = (n^2/T) \int_{\Gamma_0} \{i(\nu)/[h\nu R(\nu)/4\pi w_0 l]\} d\nu , \quad (6)$$

where the term involving the refractive index n accounts for the change in the cone angle subtended by the detector at the sample-air interface,[23] and the integral is over the emission band Γ_0. Because of the small absorption coefficients involved, reabsorption of the emission has been neglected in this analysis. Internal reflections of the incident and emitted light were not considered. The quantum efficiencies derived from Eqs. (3), (4), and (6) typically have an uncertainty of ± 10%.

E. Optical-Absorption Studies

Optical-absorption spectra of the $CdF_2:Er^{3+}$ specimens were obtained using a Cary 14 and a Cary 15 spectrophotometer. Low-temperature absorption data were obtained at 4.2 K using an immersion Dewar and at 80 K using a cold-finger Dewar.

IV. RESULTS

A. Electron Paramagnetic Resonance

1. *Angular Variation of the EPR Spectrum*

The angular dependence of the Er^{3+}-EPR spectrum arising from CdF_2: (Er^{3+}, M^+) crystals has been investigated in detail in order to test the model for the orthorhombic (C_{2v}) site proposed in Fig. 2(b) and to determine the characteristic g values. The corresponding rotation patterns for CdF_2: (Er^{3+}, U) crystals were observed to be very complex because of the superposition of spectra from Er^{3+} in several different low-symmetry sites and in sites of cubic (O_h) symmetry. Thus, a detailed analysis was not possible for these crystals.

The angular variation of the Er^{3+}-EPR spectrum arising from the lowest-lying doublet of the $^4I_{15/2}$ ground state (Sec. V A) can be treated by using an effective spin $S = \frac{1}{2}$ in the spin Hamiltonian

$$\mathcal{H} = \mu_B \vec{H} \cdot \overleftrightarrow{g} \cdot \vec{S} + \vec{I} \cdot \overleftrightarrow{A} \cdot \vec{S} , \quad (7)$$

where the first and second terms correspond to the electronic Zeeman interaction and the nuclear-hyperfine splitting, respectively. The nuclear-quadrupole interaction and the nuclear-Zeeman term have been omitted from Eq. (7), because they do not have an important influence on the results discussed in this paper.

The hyperfine term in Eq. (7) has been used only qualitatively to identify the EPR lines. For both cubic and orthorhombic Er^{3+} sites, eight hyperfine lines were observed, consistent with the nuclear spin of Er^{167} ($I = \frac{7}{2}$). In addition, the relative intensities of the hyperfine lines and the main line (arising from the even isotopes of erbium) are consistent with the isotope abundance (22.9%) of Er^{167}.

In order to characterize the local site symmetry of the (Er^{3+}, M^+) system, the angular variation of the main erbium line ($I = 0$) was determined for rotation of the magnetic field in the (110) plane of the crystal. Under these conditions, the spin Hamiltonian, Eq. (7), may be expanded in Cartesian components as follows:

$$\mathcal{H} = \mu_B (g_x H_x S_x + g_y H_y S_y + g_z H_z S_z) , \quad (8)$$

with the transitions occurring at

$$h\nu = g\mu_B H,$$

where

$$g = (l^2 g_x^2 + m^2 g_y^2 + n^2 g_z^2)^{1/2} \quad (9)$$

and l, m, and n are the direction cosines of the applied magnetic field H with respect to the g-tensor axes. The z axis, or main distortion axis of the orthorhombic site, was chosen to lie along the [110] direction, with the x axis along the [00$\bar{1}$] direction perpendicular to z, and the y axis along the [$\bar{1}$10] direction perpendicular to both x and z. For this crystal orientation (and C_{2v} symmetry), four sets of EPR lines are distinguishable on the basis of their angular variation and can be described in terms of the effective g values arising from Eq. (9)[24]:

$$g_1 = [g_x^2 \sin^2\alpha + g_z^2 \cos^2\alpha]^{1/2} , \quad (10a)$$

$$g_2 = [g_x^2 \sin^2\alpha + g_y^2 \cos^2\alpha]^{1/2} , \quad (10b)$$

$$g_3 = [\tfrac{1}{2} g_x^2 \cos^2\alpha + \tfrac{3}{4} g_y^2 \cos^2(\alpha+\delta) + \tfrac{3}{4} g_z^2 \cos^2(\alpha-\delta)]^{1/2} , \quad (10c)$$

$$g_4 = [\tfrac{1}{2} g_x^2 \cos^2\alpha + \tfrac{3}{4} g_y^2 \cos^2(\alpha-\delta) + \tfrac{3}{4} g_z^2 \cos^2(\alpha+\delta)]^{1/2} , \quad (10d)$$

where α denotes the angle between H and the [$\bar{1}$10] direction, and $\delta = \tan^{-1} 2^{1/2}$. It should be noted that

TABLE I. g values observed for Er^{3+} in C_{2v} and O_h symmetry in CdF_2. The orthorhombic g values correspond to charge compensation provided by Li^+, Na^+, Ag^+, and K^+ ions. Data were obtained at 4.2 K.[a]

Site symmetry	M^+ ion	Ionic radius (Å)[b]	g_x	g_y	g_z	$(\frac{1}{3})\mathrm{Tr}\{g\}$
C_{2v}	Li^+	0.70	5.412	5.397	9.071	6.627
	Na^+	1.00	5.898	5.882	8.274	6.685
	Ag^+	1.30	5.315	6.473	8.402	6.730
	K^+	1.37	4.999	6.564	8.333	6.632
O_h	...	...	6.759	6.759	6.759	6.759

[a]Uncertainties in the g values are ±0.005.

[b]Ionic radii are tabulated for eight fold coordination and are related to those for six fold coordination [see *Handbook of Chemistry and Physics*, 47th ed., edited by R. C. Weast and S. M. Selby (Chemical Rubber, Cleveland, Ohio, 1966), p. F124] by the factor of 1.03 [see R. C. Evans, *An Introduction to Crystal Chemistry* (Cambridge U. P., Cambridge, England, 1964), p. 44].

under these circumstances, the EPR lines corresponding to g_1 and g_2 are single, whereas those associated with g_3 and g_4 are doubly degenerate. The relative line intensities determined experimentally confirm this analysis.

The angular variations of the Er^{3+}-EPR spectra corresponding to (Er^{3+}, Na^+) and (Er^{3+}, K^+) are shown in Figs. 3(a) and 3(b), respectively, for H in the (110) crystal plane. The circles represent the experimental data. From Eq. (10), the effective g values reduce to the principal values at particular crystal orientations (i.e., $g_1 = g_z$ and $g_2 = g_y$ for $H \parallel [\bar{1}10]$ and $g_1 = g_2 = g_x$ for $H \parallel [00\bar{1}]$). The principal values of the g tensor computed from the experimental data at these two orientations are recorded in Table I for each compensating ion M^+. From these numbers it is apparent that the angular dependence of (Er^{3+}, Na^+) and (Er^{3+}, Li^+) are qualitatively very similar, as are (Er^{3+}, K^+) and (Er^{3+}, Ag^+). Thus, Na^+ and K^+ are representative of each of the two groups of compensating ions. The g values for (Er^{3+}, Na^+) and (Er^{3+}, K^+) in turn have been substituted into Eq. (10) to calculate the angular dependence shown as the solid curves in Figs. 3(a) and 3(b). Excellent agreement between the calculated curves and the experimental points is observed at all crystal orientations for each of these compensating ions. Equally good agreement was obtained for (Er^{3+}, Li^+) and (Er^{3+}, Ag^+). Similar results have been reported for Yb^{3+} and Tm^{3+} ions in orthorhombic sites.[25]

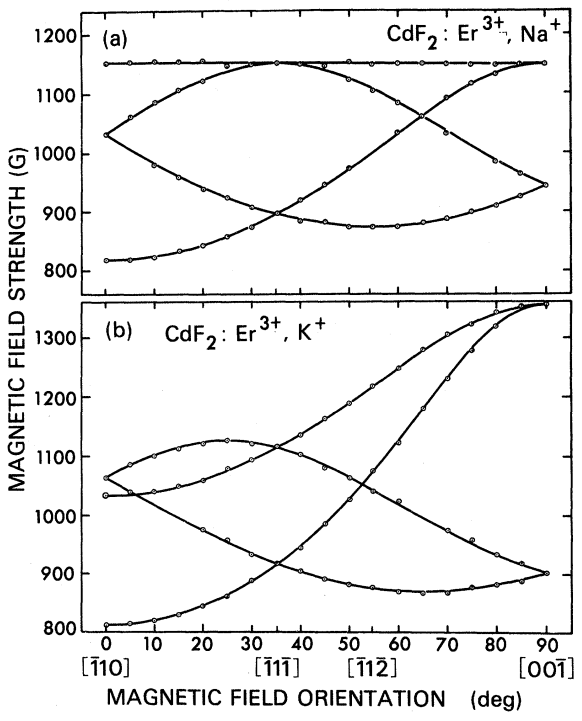

FIG. 3. Angular variation of the EPR spectrum of Er^{3+} in CdF_2 when charge compensation is provided by (a) Na^+ and (b) K^+. Data were obtained at 9.485 GHz and 4.2 K for the magnetic field in the (110) crystal plane.

2. *Distribution of Er^{3+} Sites*

In Table II the relative distribution of cubic, orthorhombic, and "other" noncubic sites are listed for (Er^{3+}, M^+) and (Er^{3+}, U) specimens. The tabulated percentages are the average values of the integrated absorption strengths obtained for the magnetic field parallel to [110] and [001] crystal directions. These results indicate that approximately one-half of the Er^{3+} ions reside in sites of C_{2v} symmetry when 1.0-mole% alkali metal fluoride (LiF, NaF, or KF) is added to the melt for charge compensation. When 1.0-mole% AgF is employed for this purpose, however, the conversion is less complete; only about 10% of the Er^{3+} ions reside in orthorhombic sites. Moreover, the total con-

TABLE II. Relative distribution of Er^{3+} local sites for $CdF_2:(Er^{3+}, U)$ and $CdF_2:(Er^{3+}, M^+)$ specimens with 0.1-mole% ErF_3.

CdF_2 crystal	Er^{3+} local sites (%)[a] Cubic O_h	Orthorhombic C_{2v}	Other noncubic[b]
(Er^{3+}, Li^+)	50	50	0.1
(Er^{3+}, Na^+)	50	50	<0.05
(Er^{3+}, Ag^+)	90	10	0.2
(Er^{3+}, K^+)	50	50	<0.05
(Er^{3+}, U)	75	...	25

[a]Uncertainties in the relative distribution are approximately ±10% of the tabulated values.

[b]Er^{3+} sites of undetermined symmetry.

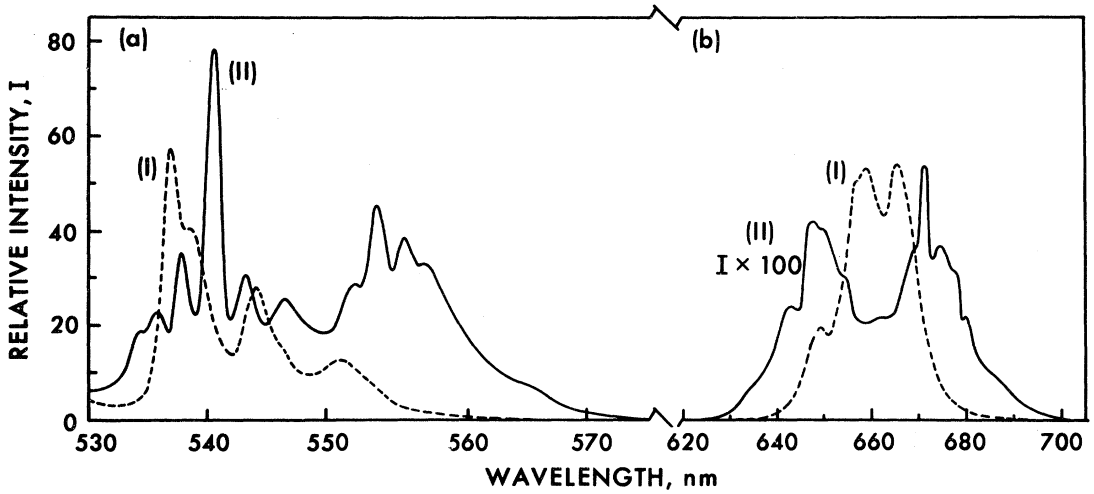

FIG. 4. Emission spectra for (a) the $^4S_{3/2} \rightarrow {}^4I_{15/2}$ transition (green) and (b) the $^4F_{9/2} \rightarrow {}^4I_{15/2}$ transition (red) corresponding to (i) CdF_2: (Er^{3+}, U) and (ii) CdF_2: (Er^{3+}, Na^+) crystals. Data were obtained at 295 K for excitation into the $^2H_{11/2}$ multiplet (Fig. 1).

centration of other noncubic sites in CdF_2 : (Er^{3+}, M^+) is more than three orders of magnitude lower than the concentration of C_{2v} sites for (Er^{3+}, Na^+) and (Er^{3+}, K^+), and approximately $\frac{1}{500}$ the concentration of O_h sites for (Er^{3+}, Li^+) and (Er^{3+}, Ag^+). These results are in contrast to CdF_2 : (Er^{3+}, U) for which EPR measurements indicate that 25% of the ions are located in several different noncubic sites of undetermined symmetry.

Several commercially grown crystals of CdF_2 (containing 0.05- and 0.5-mole% ErF_3) also were found to contain C_{2v}-Er^{3+} sites with g values corresponding to those of (Er^{3+}, Na^+) in Table I. Thus, although sodium was added to our crystals by design, it appears to be present also as an unintentional dopant in some CdF_2 crystals available commercially.

B. Optical Absorption and Emission (295 K)

1. Luminescence

The $^4S_{3/2} \rightarrow {}^4I_{15/2}$ (green) and $^4F_{9/2} \rightarrow {}^4I_{15/2}$ (red) luminescence spectra that result from excitation of the Er^{3+} ion to the $^2H_{11/2}$ level are compared in Fig. 4 for CdF_2 : (Er^{3+}, Na^+) and CdF_2 : (Er^{3+}, U). The intensity and position of emission peaks are seen to change considerably with the addition of Na^+ as a compensating ion. Crystals containing other M^+ compensating ions (Li^+, K^+, or Ag^+) produced spectra similar to that for (Er^{3+}, Na^+). For Li^+ and Ag^+ compensation, however, the 659- and 666-nm lines observed for (Er^{3+}, U) are also detectable with ~0.2% the intensity found in the (Er^{3+}, U) sample. This is consistent with the EPR results (Table II), which imply that the total number of noncubic sites in the (Er^{3+}, Li^+) and (Er^{3+}, Ag^+) samples (excluding the C_{2v} site) is ~0.5% the total observed in (Er^{3+}, U).

2. Absorption and Excitation Spectra

Comparisons of the absorption and excitation spectra of Er^{3+} in CdF_2 are helpful in distinguishing the optical properties characteristic of Er^{3+} ions in different local crystalline environments. Although the absorption spectrum is composed of contribution from all the different Er^{3+} sites, the excitation spectrum reveals only the contribution from the Er^{3+} site producing the monitored line.

Figure 5 depicts the excitation and absorption spectra for both the $^4I_{15/2} \rightarrow {}^2H_{11/2}$ (500–530 nm) and the $^4I_{15/2} \rightarrow {}^4S_{3/2}$ (530–560 nm) transitions for (Er^{3+}, U), (Er^{3+}, Na^+), and (Er^{3+}, Li^+). A $^4S_{3/2} \rightarrow {}^4I_{15/2}$ emission line is observed for all samples, while a $^4F_{9/2} \rightarrow {}^4I_{15/2}$ line is excited also in the (Er^{3+}, U) crystal. The shape and peak positions of the excitation spectra (with 4-nm resolution) are consistent with those of the absorption spectra (with 0.4-nm resolution) for (Er^{3+}, U) [Fig. 5(a)] and also for (Er^{3+}, Na^+) [Fig. 5(b)]. This correlation between the absorption and excitation spectra for the same sample implies that only one Er^{3+} site (or a group of spectrally similar Er^{3+} sites) exists in each of these specimens. On the other hand, the striking differences between the spectra produced by these two crystals indicate that they contain different kinds of optically active Er^{3+} sites. Crystals containing K^+ are spectrally similar to those containing Na^+, implying similar Er^{3+} sites. Even though the excitation spectra for (Er^{3+}, Li^+) [Fig. 5(c)] and (Er^{3+}, Ag^+) [not shown, but similar to Fig. 5(c)] are the same as for (Er^{3+}, Na^+) and (Er^{3+}, K^+), the absorption for the former group ex-

TABLE III. Lifetime τ of the $^4S_{3/2}$ and $^4F_{9/2}$ levels of Er^{3+} for various $CdF_2:Er^{3+}$ crystals.

Sample	$\tau(^4S_{3/2})$, msec 295 K	$\tau(^4S_{3/2})$, msec 77 K	$\tau(^4F_{9/2})$, msec 295 K
(Er^{3+}, Li^+)	1.5	3.2	<0.1
(Er^{3+}, Na^+)	1.8	4.6	<0.2
(Er^{3+}, Ag^+)	1.9	6.4	<0.4
(Er^{3+}, K^+)	1.7	4.8	<0.2
(Er^{3+}, U)	0.1	1.1	0.4

hibits additional lines at 516.8, 518.2, and 536.8 nm. Although the CdF_2: (Er^{3+}, Li^+) absorption spectrum appears to be an admixture of the spectra from (Er^{3+}, U) and (Er^{3+}, Na^+), the (Er^{3+}, Li^+) sample has an emission spectrum the same as that from the other (Er^{3+}, M^+) crystals (except for a barely detectable red emission discussed in Sec. IV B 1). Thus, all the (Er^{3+}, M^+) crystals share an Er^{3+} site that gives rise to common absorption and emission characteristics, as shown in Figs. 4(b) and 5(b). The strong 536.8-nm absorption band observed in (Er^{3+}, Li^+) or (Er^{3+}, Ag^+) crystals can be attributed to a second noncubic Er^{3+} site having a low quantum yield, possibly related to one of the sites observed in the (Er^{3+}, U) samples. This proposal is consistent with the EPR measurements,

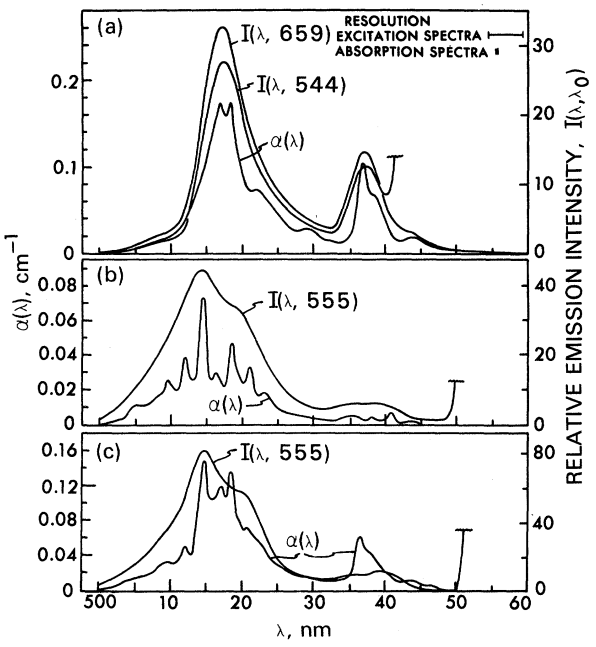

FIG. 5. Excitation spectra $I(\lambda,\lambda_0)$ and absorption spectra $\alpha(\lambda)$ where λ is the excitation wavelength, λ_0 is the monitored emission wavelength, and $\alpha(\lambda)$ is the absorption coefficient. Data were obtained at 295 K for (a) CdF_2: (Er^{3+}, U), (b) CdF_2: (Er^{3+}, Na^+), and (c) CdF_2: (Er^{3+}, Li^+) crystals.

which reveal the existence of weak noncubic Er^{3+} spectra (different from the orthorhombic Er^{3+} spectra) in both the (Er^{3+}, Li^+) and (Er^{3+}, Ag^+) samples (Table II).

3. *Lifetimes*

The lifetimes τ observed at 295 K for the $^4S_{3/2}$ and $^4F_{9/2}$ levels are shown in Table III for (Er^{3+}, M^+) and (Er^{3+}, U) crystals. The lifetimes observed at 77 K are also tabulated for the $^4S_{3/2}$ level. As for the absorption, excitation, and emission measurements discussed above, the (Er^{3+}, M^+) specimens gave consistent lifetimes that differed considerably from those for (Er^{3+}, U). As expected, the lifetimes of the $^4S_{3/2}$ state all increased at liquid-nitrogen temperatures. The most drastic change was observed for the (Er^{3+}, U) crystal.

4. *Quantum Yields*

The radiative quantum yield $\eta^R(E_j \rightarrow E_k)$ for the transition $E_j \rightarrow E_k$ is defined as the number of ions which, when excited to state E_j, decay radiatively to E_k (η without the superscript R defines the total-quantum yield). The η's are related to the experimentally determined $Q(\Gamma_i, \Gamma_0)$ defined in Eq. (3) by

$$\eta(^4S_{3/2} \rightarrow {}^4F_{9/2}) = \frac{Q(^4I_{15/2} \rightarrow {}^4S_{3/2},\ {}^4F_{9/2} \rightarrow {}^4I_{15/2})}{Q(^4I_{15/2} \rightarrow {}^4F_{9/2},\ {}^4F_{9/2} \rightarrow {}^4I_{15/2})}\ , \tag{11a}$$

$$\eta^R(E_j \rightarrow {}^4I_{15/2}) = Q(^4I_{15/2} \rightarrow E_j,\ E_j \rightarrow {}^4I_{15/2})\ . \tag{11b}$$

Table IV lists $\eta^R(^4S_{3/2} \rightarrow {}^4I_{15/2})$, $\eta^R(^4F_{9/2}, {}^4I_{15/2})$, and $\eta(^4S_{3/2} \rightarrow {}^4F_{9/2})$ for the (Er^{3+}, Na^+), (Er^{3+}, K^+), and (Er^{3+}, U) samples. The quantum yields for (Er^{3+}, Li^+) or (Er^{3+}, Ag^+) are comparable to those containing the other two M^+ ions, but overlapping absorption in the spectra for (Er^{3+}, Li^+) and (Er^{3+}, Ag^+) (Sec. IV B 2) produces considerable uncertainty in η. The addition of M^+ ions into CdF_2: Er^{3+} is seen to cause an order of magnitude increase in $\eta^R(^4S_{3/2} \rightarrow {}^4I_{15/2})$ and a similar order of magnitude decrease in $\eta^R(^4F_{9/2} \rightarrow {}^4I_{15/2})$. The quantum yield for the $^4S_{3/2} \rightarrow {}^4F_{9/2}$ transition also decreases as a result of M^+ compensation. It was also established that $\eta(^2H_{11/2} \rightarrow {}^4S_{3/2}) = \eta(^4S_{3/2} \rightarrow {}^2H_{11/2}) = 1$, indicating that the $^2H_{11/2}$ and $^4S_{3/2}$ multiplets thermalize in a time short compared

TABLE IV. Radiative quantum yield for decay from the $^4S_{3/2}$ and $^4F_{9/2}$ states to the $^4I_{15/2}$ ground state, and the total yield for $^4S_{3/2}$ to $^4F_{9/2}$ decay for various CdF_2: Er^{3+} crystals. Data were obtained at 295 K.

Sample	Quantum yield η (%) $^4S_{3/2} \rightarrow {}^4I_{15/2}$	$^4F_{9/2} \rightarrow {}^4I_{15/2}$	$^4S_{3/2} \rightarrow {}^4F_{9/2}$
(Er^{3+}, Na^+)	19.7	2.9	38
(Er^{3+}, K^+)	20.4	3.6	35
(Er^{3+}, U)	2.3	26	80

TABLE V. Radiative transition rate corresponding to the $^4S_{3/2}$ and $^4F_{9/2}$ to $^4I_{15/2}$ transitions, and the total rate for the $^4S_{3/2}$ to $^4F_{9/2}$ transition for various CdF_2: Er^{3+} crystals. Data are tabulated for 295 K.

Sample	Transition rate W (sec^{-1}) $^4S_{3/2} \rightarrow {}^4I_{15/2}$	$^4F_{9/2} \rightarrow {}^4I_{15/2}$	$^4S_{3/2} \rightarrow {}^4F_{9/2}$
(Er^{3+}, M^+)[a]	120	>340	220
(Er^{3+}, U)	230	650	8000

[a] W are obtained from the average τ and η provided in Tables III and IV, respectively.

with their lifetime. This result is not unexpected since the energy gap between these two multiplets is only $3.5kT$ (700 cm^{-1}) at room temperature.

5. *Transition Rates*

The transition rate $W(E_j \rightarrow E_k)$ is the probability per second that an ion in state E_j will decay to state E_k. Table V lists the transition rates obtained from the relation

$$W(E_j \rightarrow E_k) = \eta(E_j \rightarrow E_k)/\tau(E_j) , \qquad (12)$$

where the lifetimes and quantum yields are given in Tables III and IV. The average transition rates are shown for the CdF_2: (Er^{3+}, M^+) samples. Although the addition of M^+ decreases somewhat the radiative-decay probabilities to the ground state, the major decrease (36-fold) occurs for the $^4S_{3/2} \rightarrow {}^4F_{9/2}$ transition. A more detailed discussion in terms of multiphonon decay processes is postponed until Sec. V B.

C. Low-Temperature Optical Spectra

1. $^4S_{3/2} \rightleftarrows {}^4I_{15/2}$ *Spectra*

In order to determine the crystal-field splitting of the $^4I_{15/2}$ ground state of Er^{3+} in CdF_2: (Er^{3+}, M^+), low-temperature emission spectra (77 and 4.2 K) and absorption spectra (4.2 K) were obtained for the $^4S_{3/2} \rightleftarrows {}^4I_{15/2}$ transition. The $^4S_{3/2}$ multiplet is the simplest excited state of Er^{3+}, consisting of two levels in a noncubic crystalline field. The $^4I_{15/2}$ multiplet has eight levels in a noncubic field (Sec. V A). The 77-K emission is shown in Fig. 6 for CdF_2: (Er^{3+}, U) and in Figs. 7(a)–7(d) for CdF_2: (Er^{3+}, M^+). The spectra in Fig. 7 are arranged in order of increasing M^+ ionic radii. Striking differences are observed between the spectra of the (Er^{3+}, U) and the (Er^{3+}, M^+) crystals. In the region 18 300–18 400 cm^{-1}, sharp electronic lines present for the (Er^{3+}, U) crystal are absent for the (Er^+, M^+) samples, and the converse is true in the 17 900–18 100 cm^{-1} region. The sharp electronic lines are numbered in Fig. 7. Vibronic emission bands can be discerned for the (Er^{3+}, M^+) spectra in the regions 18 100–18 450 cm^{-1} and 17 500–18 000 cm^{-1}, with Stokes shifts consistent with the reported[26] TO (224 cm^{-1}) and LO (403 cm^{-1}) phonon energies of CdF_2. For (Er^{3+}, U) the vibronic band at 18 000 to 18 200 cm^{-1} (Stokes shifted from the electronic lines at 18 300 to 18 400 cm^{-1}) corresponds to the emission of TO phonons. The higher-energy LO phonons are not observed in this crystal. The intensities of the vibronic bands shown in Fig. 7 increase monotonically with M^+ ionic radii. This behavior is consistent with the regular variation in the width of the room-temperature emission lines as the compensating M^+ ion is changed.

On cooling the M^+ compensated samples to 4.2 K, the emission lines designated by a prime in Fig. 7 disappear. The absorption spectra of the CdF_2: (Er^{3+}, M^+) crystals at 4.2 K consist of lines corresponding in energy to emission lines 1 and 1′. Additional lines are present in the (Er^{3+}, Li^+) and (Er^{3+}, Ag^+) absorption spectra, but these do not correspond to any of the observed emission lines. Because there are only two $^4S_{3/2}$ levels and only the lowest level of the $^4I_{15/2}$ multiplet is populated at 4.2 K, only two absorption lines are possible for each Er^{3+} site. Thus, (Er^{3+}, Na^+) and (Er^{3+}, K^+) have only one type of Er^{3+} site, while (Er^{3+}, Li^+) and (Er^{3+}, Ag^+) have more than one. The additional lines in the latter samples may be attributed to the Er^{3+} site with low quantum efficiency (Sec. IV B 2) observed at room temperature. The low-temperature emission thus arises from sites common to all CdF_2: (Er^{3+}, M^+) crystals.

2. $^4I_{15/2}$ *Crystal Field Splitting*

The (Er^{3+}, M^+) $^4S_{3/2} \rightarrow {}^4I_{15/2}$ spectra consist of two series of eight lines each. The primed series 1′, 2′, . . . , 8′ correspond to transitions from the upper level $E2$ of the $^4S_{3/2}$ multiplet to the $Z1$, $Z2, \ldots, Z8$ levels of the $^4I_{15/2}$ multiplet, respec-

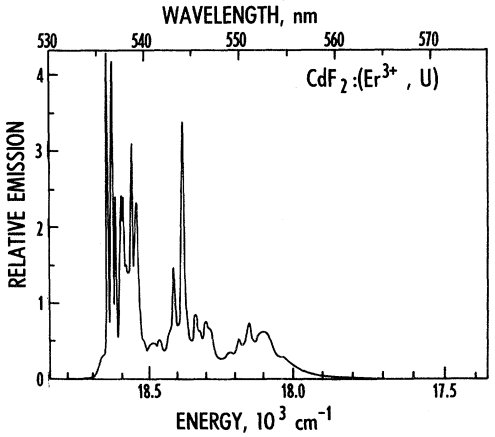

FIG. 6. Emission spectra obtained at 77 K for the $^4S_{3/2} \rightarrow {}^4I_{15/2}$ transition in CdF_2: (Er^{3+}, U).

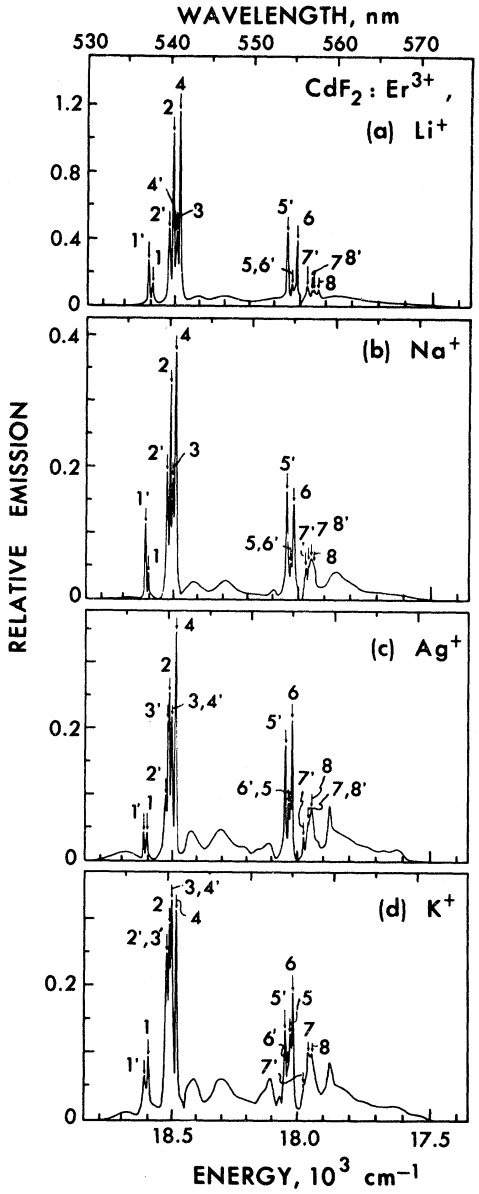

FIG. 7. Emission spectra obtained at 77 K for the $^4S_{3/2} \rightarrow {}^4I_{15/2}$ transition in CdF_2: (Er^{3+}, M^+), where M^+ is (a) Li^+, (b) Na^+, (c) Ag^+, and (d) K^+. The electronic lines that are numbered are identified in the text.

tively. Similarly the unprimed series results from decay of the lower $^4S_{3/2}$ level $E1$ to the $^4I_{15/2}$ ground state. The 4.2-K absorption and emission data reveal that only the levels $Z1$ and $E1$ (after excitation) have an appreciable population at this temperature, and they are therefore the lowest energy states of their respective multiplets. Table VI lists the energies of the two series of lines $E(Z_i)$ given by the average of $(h\nu_1 - h\nu_i)$ and $(h\nu_{1'} - h\nu_{i'})$. For the two $^4S_{3/2}$ levels the energies are $E(E1) = h\nu_1$ and $E(E2) = h\nu_{1'}$. The uncertainty in $E(Z_i)$ is ± 0.4 cm^{-1} except for $Z7$ and $Z8$, which are obtained from transitions partially obscured by vibronic bands.

V. DISCUSSION

A. Nature of the Orthorhombic Crystalline Field in $CdF_2:(Er^{3+}, M^+)$

Attempts at optical characterization of charge-compensated rare-earth ion sites in crystals exhibiting the fluorite structure have been plagued by the inability to isolate and identify positively a particular site from among the numerous sites usually present. $CdF_2:(Er^{3+}, M^+)$ is one crystal in which isolation of a specific site (the orthorhombic-Er^{3+} site) has been achieved. The EPR measurements have shown that the C_{2v}-Er^{3+} site accounts for >99.8% of the noncubic sites in the (Er^{3+}, Li^+), (Er^{3+}, Na^+), and (Er^{3+}, K^+) samples and approximately 98.0% in the (Er^{3+}, Ag^+) sample (Table II). In this discussion the EPR and optical properties that have been correlated with the orthorhombic-Er^{3+} site are used to analyze the detailed nature of this optically active center.

From the point-charge crystal field model, the electrostatic potential energy V, for a crystal field of C_{2v} symmetry (at the Er^{3+} ion) takes the form[27]

$$V(C_{2v}) = B_2^0 O_2^0 + B_2^2 O_2^2 + B_4^0 O_4^0 + B_4^2 O_4^2 + B_4^4 O_4^4 + B_6^0 O_6^0 + B_6^2 O_6^2 + B_6^4 O_6^4 + B_6^6 O_6^6 \ , \quad (13)$$

where the functions O_n^m are equivalent to terms of a spherical harmonic expansion of the crystal field (within a manifold of constant J). The parameters B_n^m describe the strength of the crystal field perturbation and are directly related to the more common $A_n^m \langle r^n \rangle$ parameters.[19]

The potential $V(C_{2v})$ contains nine different B_n^m parameters, and it is clear that the unequivocal determination of these coefficients would be possible only by fitting very extensive experimental data. Fortunately, in the case of (Er^{3+}, M^+), the exact solution of Eq. (13) is not necessary. The EPR and optical measurements indicate that the C_{2v} – Er^{3+} site produced by M^+ compensation is not greatly perturbed from the cubic site (O_h symmetry). In particular, the C_{2v} site produced by Li^+ or Na^+ can be approximated quite adequately in terms of a large cubic-field potential perturbed by a smaller axial-field term. For K^+ and Ag^+, on the other hand, the nonaxial (orthorhombic) perturbation must also be considered.

1. Cubic Field

Trivalent erbium has eleven $4f$ electrons, and the ground state of the free ion is $^4I_{15/2}$. In a cubic crystalline field, the 16-fold degeneracy of the ground state splits into $3\Gamma_8$ quartets, a Γ_6 doublet and a Γ_7 doublet. For Er^{3+} in O_h symmetry in CdF_2, the Γ_7 state has been shown[28] to lie lowest,

TABLE VI. Crystal field splitting of the $^4I_{15/2}$ ground state of Er^{3+} in CdF_2, compensated by a monovalent cation M^+. $E(Z_i)$ were calculated from the luminescence spectra of the $^4S_{3/2} \rightarrow {}^4I_{15/2}$ transition, obtained at 77 K. Parentheses indicate those values of $h\nu$, $h\nu'$, and $E(Z_i)$ where uncertainties exist (e.g., arising from line broadening).

Energy level, Z_i	$h\nu$[a] cm^{-1}	$h\nu'$[a] cm^{-1}	$E(Z_i)$ cm^{-1}	Energy level, Z_i	$h\nu$[a] cm^{-1}	$h\nu'$[a] cm^{-1}	$E(Z_i)$ cm^{-1}
Li^+ 1	18598.1	18615.9	0	Ag^+ 1	18601.5	18616.2	0
2	18511.8	18528.6	86.8	2	18512.0	18526.4	89.7
3	18495.9	...	102.2	3	18502.4	18517.1	99.1
4	18483.4	18500.7	115.0	4	18485.3	18499.7	116.4
5	18035.9	18052.8	562.7	5	(18031.7)	18045.0	571.2
6	18016.1	18032.3	582.8	6	18017.7	(18031.7)	583.8
7	17959.1	17977.2	638.9	7	...	17973.0	643.2
8	17935.0	17952.0	663.5	8	17943.7	...	657.8
Na^+ 1	18603.3	18615.7	0	K^+ 1	18600.7	18619.0	0
2	18513.2	18525.0	90.4	2	18509.9	18527.3	91.3
3	18502.8	...	100.5	3	18503.1	18521.3	97.7
4	18491.5	...	111.8	4	18482.2	18500.4	118.6
5	(18032.6)	18044.7	571.0	5	(18026.2)	18046.5	572.5
6	18017.0	(18029.4)	586.3	6	18013.8	(18034.3)	586.9
7	(17959.4)	17971.4	644.3	7	17958.2	17975.9	642.8
8	(17941.4)	(17950.7)	(663.5)	8	(17943.7)	...	(657.0)

[a] $h\nu$ and $h\nu'$ correspond to wave numbers in air.

as established by the g values (see Table I). The relative positions of the higher-lying energy levels are a function of the fourth- and sixth-order terms of the cubic potential

$$V(O_h) = B_4 (O_4^0 + 5O_4^4) + B_6(O_6^0 - 21O_6^4) , \qquad (14)$$

which have been plotted by Lea, Leask, and Wolf[19] (hereinafter referred to as LLW) in a particularly convenient way. The LLW formalism defines two parameters W and x, such that

$$B_4 F(4) = Wx \quad \text{and} \quad B_6 F(6) = W(1 - |x|) , \qquad (15)$$

where W is an energy-scale factor and x (between -1 and $+1$) is determined by the ratio B_4/B_6. For $J = \frac{15}{2}$, $F(4)$ and $F(6)$ are 60 and 13 860, respectively. Using this formalism, we have reconstructed the $^4I_{15/2}$ multiplet structure for CdF_2: (Er^{3+}, M^+) crystals consistent with the experimentally determined energies in Table VI. These results are recorded in Table VII, and they stem from the following reasoning.

From Table I, we observe that $\frac{1}{3}\mathrm{Tr}\{g\}$ for the (Er^{3+}, M^+) crystals agrees well with the g value obtained for Er^{3+} in a cubic site. This implies the departure from O_h symmetry is small (Sec. V A 2) and that the C_{2v}-Er^{3+} spectra arise from the Γ_7 doublet.[29] From LLW, a Γ_7 ground state imposes the constraint that $-0.46 \leq x \leq 0$, which in turn implies a distribution of $^4I_{15/2}$ energy levels that is found to be consistent with the luminescence data (i.e., a low-lying group of three energy levels and a higher-lying group of two levels). Moreover, we obtain a preliminary labeling of the energy levels recorded in Table VI, the only uncertainty being the relative positions of $\Gamma_8^{(1)}$ and Γ_6. The parameters x and W have been determined from LLW to provide the best fit to the experimental separations (Table VII) between the Γ_7, $\Gamma_8^{(2)}$, and $\Gamma_8^{(3)}$ states. Values of $E(\Gamma_8^{(3)}) = 651.4$ cm^{-1} and $E(\Gamma_8^{(2)}) = 577.2$ cm^{-1} corresponding to the average of the four (Er^{3+}, M^+) samples, lead to $x = -0.36$ and $W = 1.810$ cm^{-1}. Thus, the cubic approximation of the C_{2v}-Er^{3+} site provides an excellent fit to the Γ_7, $\Gamma_8^{(2)}$, and $\Gamma_8^{(3)}$ energy levels, and predicts the approximate positions of the $\Gamma_8^{(1)}$ and Γ_6 states. The small discrepancies between the calculated and measured values for these latter two states can be accounted for qualitatively in terms of an axial-field perturbation. Using the above values of x and W to calculate B_4 and B_6, the crystal field parameters for Er^{3+} are $A_4\langle r^4\rangle$

TABLE VII. Crystal field splitting of the $^4I_{15/2}$ ground state as calculated (from LLW) and measured in CdF_2: (Er^{3+}, M^+) crystals.

Energy level	Cubic approximation Γ	E, cm^{-1}	Measured energy[a] (cm^{-1})/M^+ ion Li^+	Na^+	Ag^+	K^+
1	Γ_7	0	0	0	0	0
2,3	$\Gamma_8^{(1)}$	101.4	94.5	95.5	94.4	94.5
4	Γ_6	108.6	115.0	111.8	116.4	118.6
5,6	$\Gamma_8^{(2)}$	578.3	572.8	578.7	577.5	579.7
7,8	$\Gamma_8^{(3)}$	650.7	651.2	653.9	650.5	649.9

[a] The energies tabulated for the Γ_8 states are the means of the energies derived from experiment (see Table VI).

$= -245\ cm^{-1}$ and $A_6\langle r^6\rangle = 40\ cm^{-1}$.

The success of the cubic approximation for the C_{2v} site has certain implications regarding the luminescence spectra depicted in Fig. 6 for $CdF_2:(Er^{3+},U)$. For these samples, transitions corresponding to energies between 18300 and 18400 cm^{-1} were observed, but were absent for (Er^{3+},M^+) specimens. In terms of the LLW formalism (and $-0.46 \leq x \leq 0$), even a poor fit to these lines is not possible. This implies that these transitions probably arise from Er^{3+} in highly distorted, low-symmetry sites (consistent with the EPR measurements).

2. Axial Field

In light of the g values for $CdF_2:(Er^{3+},M^+)$ recorded in Table I, it is reasonable to assume that the noncubic portion of the total crystal field may be approximated by an axial distortion along the $\langle 110\rangle$ direction parallel to the Er^{3+}-M^+ axis (the z axis). Because the separation $(\Gamma_8^{(1)} - \Gamma_7)$ is large ($\sim 100\ cm^{-1}$) compared to the noncubic perturbation ($\sim 10\ cm^{-1}$), first-order perturbation theory is expected to be valid. A straightforward perturbation calculation leads to anisotropic g values of the following form[30]:

$$g_{\parallel} = g_c - 2\,\frac{kV}{E(\Gamma_8^{(1)})_{\parallel} - E(\Gamma_7)}\ , \tag{16a}$$

$$g_{\perp} = g_c + \frac{kV}{E(\Gamma_8^{(1)})_{\perp} - E(\Gamma_7)}\ , \tag{16b}$$

where g_c is the cubic g value, V is the axial potential, and k is a constant which reflects the specific crystal field. $(\Gamma_8^{(1)})_{\parallel}$ and $(\Gamma_8^{(1)})_{\perp}$ are components of $\Gamma_8^{(1)}$ that couple to Γ_7 for $H \parallel z$ and $H \perp z$, respectively. From Table I, $g_{\perp} < g_c < g_{\parallel}$ [where $g_{\perp} \equiv \frac{1}{2}(g_x + g_y)$ and $g_{\parallel} \equiv g_z$] and thus $kV < 0$. Combining Eqs. (16a) and (16b),

$$g_{\parallel} + 2g_{\perp} = 3g_c - 2kV \times\left(\frac{1}{E(\Gamma_8^{(1)})_{\parallel} - E(\Gamma_7)} - \frac{1}{E(\Gamma_8^{(1)})_{\perp} - E(\Gamma_7)}\right). \tag{17}$$

If the difference term within the brackets is small, one-third the trace of the anisotropic g values is very nearly equal to the cubic g value. Table I shows this approximate equality for all (Er^{3+},M^+) samples which implies that the ground-state wave functions corresponding to these C_{2v}-Er^{3+} sites are not very different from those of a Γ_7 doublet. The equality is not exact, however, $3g_c > g_{\parallel} + 2g_{\perp}$ for each of the compensating ions in Table I. Thus Eq. (17) implies (for $kV < 0$) that $E(\Gamma_8^{(1)})_{\parallel}$ corresponds to level 3 (in Table V) and lies higher than $E(\Gamma_8^{(1)})_{\perp}$ (level 2).

Moreover, Γ_6 and $(\Gamma_8^{(1)})_{\perp}$ will interact through an axial field and therefore will be mutually repelled. In fact, a small repulsion corresponding to $\sim 6\ cm^{-1}$ would account for the differences between calculated and measured values recorded in Table VII. In this discussion we have neglected the coupling between the Γ_7 ground state and the $\Gamma_8^{(1)}$ state.

In order to test the validity of the axial field as an approximation to the C_{2v} symmetry of the (Er^{3+},M^+) site, Eq. (16) can be employed to write an expression relating the EPR g values to the energy level separations determined from luminescence studies,

$$\frac{2|g_{\perp} - g_c|}{|g_{\parallel} - g_c|} = \frac{E(\Gamma_8^{(1)})_{\parallel}}{E(\Gamma_8^{(1)})_{\perp}}\ . \tag{18}$$

The above quantity has been computed for each of the (Er^{3+},M^+) samples using data from Tables I and VI, with the results shown in Table VIII. The excellent agreement attained provides additional confirmation that the C_{2v}-Er^{3+} site characterized by EPR is responsible for the Er^{3+} optical properties summarized in Tables III–VI. Moreover, the correlation between the quantities recorded in Table VIII and the radii of the M^+ ions supports strongly the concept that an axial distortion along the Er^{3+}-M^+ direction is a satisfactory approximation for the C_{2v}-Er^{3+} site, especially for Li^+ or Na^+ compensation. In particular, the Na^+ ion fits snugly into the Cd^{2+} position ($r = 1.00$ Å), whereas the Li^+ ion fits quite loosely. As a result, the Li^+ can undergo a displacement along z by as much as 12% (0.5 Å) without greatly disturbing its adjacent fluorine neighbors. The direction of the displacement would be toward the Er^{3+} ion, because the Er^{3+} and Li^+ have effective charges of opposite sign. This model for (Er^{3+},Li^+) is consistent with its greater g-value anisotropy and, in turn, with its greater Γ_8 splittings, as compared to (Er^{3+},Na^+).

3. Orthorhombic Field

As evidenced by the g values for (Er^{3+},Ag^+) and (Er^{3+},K^+) (Tables I and VIII), the orthorhombic contribution to the crystal field must be included for these samples. This additional distortion is not unexpected, because Ag^+ and K^+ are both ~30% larger than Cd^{2+}. The introduction of these ions

TABLE VIII. Correlation of the EPR and optical results in terms of an axial-field approximation.

M^+ ion	$\dfrac{E(\Gamma_8^{(1)})_{\parallel}}{E(\Gamma_i^{(1)})_{\perp}}$	$\dfrac{2\lvert g_{\perp} - g_c\rvert}{\lvert g_{\parallel} - g_c\rvert}$ [a]
Li^+	1.18	1.17
Na^+	1.11	1.15
Ag^+	1.11	1.05
K^+	1.07	1.24

[a] $g_{\perp} \equiv \frac{1}{2}(g_x + g_y)$ and $g_{\parallel} \equiv g_z$ (see Table I).

would be expected to lead to some distortion of the adjacent fluorine ions, in the simplest case causing the F^- to F^- separation to increase along a $\langle 100 \rangle$ crystal direction. Such a distortion would cause the x and y axes to become inequivalent and make $g_x \neq g_y$, in agreement with the EPR measurements.

B. Multiphonon Decay Processes

The most dramatic difference between the spectra of the CdF_2 : (Er^{3+}, U) and CdF_2 : (Er^{3+}, M^+) crystals is the large variation in the relative intensity of the red $({}^4F_{9/2} \rightarrow {}^4I_{15/2})$ and green $({}^4S_{3/2} \rightarrow {}^4I_{15/2})$ emission. Similar variations are observed for Er^{3+} ions in different hosts[31] and in different crystalline environments in the same host.[17] In CdF_2, the relatively efficient green emission of (Er^{3+}, M^+) is quenched in (Er^{3+}, U) by an enhanced ${}^4S_{3/2} \rightarrow {}^4F_{9/2}$ transition rate (Table V). Preliminary measurements of transition rates from the ${}^4F_{9/2}$ level indicate that the red efficiency probably is degraded by an enhanced ${}^4F_{9/2} \rightarrow {}^4I_{9/2}$ decay rate. For SrF_2, the ${}^4S_{3/2} \rightarrow {}^4F_{9/2}$ transition rate has been analyzed in terms of multiphonon decay across a 3000-cm^{-1} gap.[32] This transition in CdF_2 probably is due to multiphonon processes also, because the phonon spectra for these two hosts are similar,[33] and the transition rate $W({}^4S_{3/2} \rightarrow {}^4I_{15/2})$ for SrF_2 (235 sec^{-1}) agrees with the rate for CdF_2 : (Er^{3+}, M^+) (220 sec^{-1}, from Table V).

A phenomenological analysis of the multiphonon-decay process has been made by Riseberg and Moos[32] (hereinafter referred to as RM). Their treatment assumes that the detailed features of the interacting phonon modes and atomic levels are averaged out, and that the only critical parameter for a given host is the energy gap E_g. The decay occurs in approximately the lowest order permitted by energy conservation (i.e., the energy of the phonons involved is near the cutoff of the phonon spectrum). The phonon cutoff energy $\hbar\omega_m$ refers to the highest-energy phonon observed in the vibronic spectra and thus is related to the orbit-lattice interaction. However, because this interaction, and therefore $\hbar\omega_m$, may vary for different Er^{3+} sites, the order of the process $(n = E_g/\hbar\omega_m)$ may also vary even for the same energy gap E_g. Thus, in crystalline lattices where more than one Er^{3+} site may exist, as in CdF_2, parameters other than E_g need to be specified.

The phonon cutoff energy can be estimated from the 77-K emission spectra (Figs. 6 and 7) discussed in Sec. IV C. Phonons corresponding to a LO phonon energy of 403 cm^{-1} are observed in the (Er^{3+}, M^+) samples, but are absent in the (Er^{3+}, U) specimens for which the maximum phonon energy is approximately 300 cm^{-1}. Thus, the multiphonon decay across a 3000-cm^{-1} gap involves $n = 10$ phonons, $\hbar\omega_m = 300$ cm^{-1} for (Er^{3+}, U) and $n = 8$ phonons, $\hbar\omega_m = 375$ cm^{-1} for (Er^{3+}, M^+). The temperature dependence of the decay rate is related to the order of the process and will change for different types of Er^{3+} sites. The transition rate, considering both stimulated and spontaneous phonon emission,[32] is

$$W(T) = W_0 (1 - e^{-\hbar\omega_m / kT})^{-n} , \tag{19}$$

where W_0 is the spontaneous (low-temperature) rate. For the (Er^{3+}, U) and (Er^{3+}, M^+) samples $W(295)/W(77) \approx W(295)/W_0$ is 14 and 4, respectively. These values are consistent with the experimental lifetimes in Table III, assuming that the temperature dependence of $\tau({}^4S_{3/2})$ and $W({}^4S_{3/2} \rightarrow {}^4F_{9/2})$ are similar. Thus, the order n of the multiphonon-decay process in CdF_2 is a function of the Er^{3+} site.

The RM analysis shows also that the spontaneous emission rate depends exponentially upon the order of the process:

$$W_0 = A\epsilon^n , \tag{20}$$

where A is a constant and ϵ is the coupling parameter that reflects the strength of the orbit-lattice interaction. From Table III, the 77-K rates for two different CdF_2 crystals are comparable, but n differs, implying that ϵ also must depend upon the nature of the Er^{3+} local site. If, for example, $\epsilon = 0.20$ for CdF_2 : (Er^{3+}, M^+), as for SrF_2 : Er^{3+},[32] and $W_0(Er^{3+}, U)/W_0(Er^{3+}, M^+) = \tau(Er^{3+}, M^+)/\tau(Er^{3+}, U) \approx 4$, then $\epsilon = 0.32$ for CdF_2 : (Er^{3+}, U). The larger coupling factor for the (Er^{3+}, U) crystal is consistent with a stronger noncubic crystal field at the Er^{3+} ion, in contrast to the "nearly" cubic Er^{3+} sites observed in the (Er^{3+}, M^+) samples (Sec. V A).

Thus, the multiphonon decay rates in a given host depend not only upon the energy gap, as is commonly assumed, but also upon parameters that reflect the specific nature of the crystalline environment of the optically active ion.

VI. SUMMARY

The EPR spectrum of Er^{3+} in CdF_2 compensated by M^+ ions has been investigated and shown to arise from Er^{3+} in C_{2v} symmetry, consistent with a monovalent cation substituting for a nearest neighbor Cd^{2+} ion [Fig. 2(b)]. These Er^{3+} sites have been shown to account for nearly all (>98%) of the noncubic spectra recorded for CdF_2 : (Er^{3+}, M^+) crystals. As a result, we have been able to characterize unambiguously the optical properties of Er^{3+} in C_{2v} symmetry. Four M^+ compensating ions (Li^+, Na^+, Ag^+, and K^+) have been shown to give rise to similar Er^{3+} luminescence, absorption, and excitation spectra, in contrast to those spectra obtained for CdF_2 : (Er^{3+}, U). Lifetimes of the ${}^4S_{3/2}$ state of Er^{3+}, radiative-quantum yields (in the green and red) and transition rates from the

$^4S_{3/2}$ and $^4F_{9/2}$ states have also been shown to be similar for each M^+ ion used for compensation, but again, to differ from the results obtained for Er^{3+} in $CdF_2:(Er^{3+},U)$ specimens.

The crystal field splitting of the $^4I_{15/2}$ ground state of Er^{3+} (obtained from the luminescence data for Er^{3+} in C_{2v} symmetry) can be accounted for remarkably well in terms of the cubic-field approximation of LLW. An axial-field perturbation along the Er^{3+}-M^+ direction is consistent with the EPR g values and with the relative magnitudes of the $\Gamma_8^{(1)}$ splitting observed experimentally. The axial distortion is greatest for (Er^{3+},Li^+); however, the magnitude of the crystal field (and the ratio of fourth- to sixth-order cubic terms) was found to be approximately constant throughout the M^+ series. Discrepancies from the axial-field description are greatest for Ag^+ and K^+ compensating ions, implying that the orthorhombic contribution to the total crystal field is largest for these cations.

The relative intensity of red to green emission has been observed to be a sensitive function of the local-site symmetry of the Er^{3+} ion. These differences can be accounted for on the basis of differences in multiphonon decay processes, which in turn depend upon the crystal field at the Er^{3+} ion.

ACKNOWLEDGMENTS

The authors express their gratitude to H. P. R. Frederikse and the other members of the Solid State Physics Section at the National Bureau of Standards for their cooperation in this research effort, especially for the use of some experimental equipment. In particular, it is a pleasure to thank W. R. Hosler for the excellent CdF_2 crystals used in this study. The authors, have benefited from stimulating discussions with members of the Physics Department at RIAS. R. G. Lye and S. E. Stokowski have been most helpful with their critical analyses of this paper. Particular thanks are due to W. Holton for his competent assistance in the experimental program.

[1]J. M. Baker, W. Hayes, and D. A. Jones, Proc. Phys. Soc. (London) 73, 942 (1959).

[2]M. Dvir and W. Low, Proc. Phys. Soc. (London) 75, 136 (1960).

[3]U. Ranon and W. Low, Phys. Rev. 132, 1609 (1963).

[4]M. J. Weber and R. W. Bierig, Phys. Rev. 134, A1492 (1964).

[5]M. R. Brown, K. G. Roots, I. M. Williams, W. A. Shand, C. Groter, and H. F. Kay, J. Chem. Phys. 50, 891 (1969).

[6]G. M. Zverev and A. I. Smirnov, Fiz. Tverd. Tela 6, 96 (1964) [Sov. Phys. Solid State 6, 76 (1964)].

[7]Yu. A. Bobrovnikiv, G. M. Zverev and A. I. Smirnov, Fiz. Tverd. Tela 8, 2205 (1966) [Sov. Phys. Solid State 8, 1750 (1967)].

[8]A. A. Antipun, I. N. Kurkin, L. D. Livanova, L. Z. Potvorova, and L. Ya. Shekun, Fiz. Tverd. Tela 8, 2664 (1966) [Sov. Phys. Solid State 8, 2130 (1967)].

[9]N. E. Byer, T. C. Ensign, and W. M. Mularie, Appl. Phys. Letters 20, 286 (1972).

[10]N. E. Byer, T. C. Ensign, and W. M. Mularie, Bull. Am. Phys. Soc. 17, 310 (1972).

[11]T. C. Ensign, N. E. Byer, and W. M. Mularie, Bull. Am. Phys. Soc. 17, 310 (1972).

[12]S. A. Pollack, J. Chem. Phys. 40, 2751 (1964).

[13]Yu. K. Voron'ko, G. M. Zverev, B. B. Meshkov, and A. I. Smirnov, Fiz. Tverd. Tela 6, 2799 (1964) [Sov. Phys. Solid State 6, 2225 (1965)].

[14]J. Kirkton and S. D. McLaughlan, Phys. Rev. 155, 279 (1967).

[15]C. W. Rector, B. C. Pandey, and H. W. Moos, J. Chem. Phys. 45, 171 (1966).

[16]Yu. K. Voron'ko, A. A. Kaminskiĭ, and V. V. Osiko, Zh. Eksperim. i Teor. Fiz. 50, 15 (1966) [Sov. Phys. JETP 23, 10 (1966)].

[17]For example: I. V. Stepanov and P. P. Feofilov, Dokl. Akad. Nauk SSSR 108, 615 (1955) [Sov. Phys. Doklady 1, 350 (1956)]; Ref. 7.

[18]I. B. Aizenberg, L. D. Livanova, I. G. Saitkulov, and A. L. Stolov, Fiz. Tverd. Tela 10, 2030 (1968) [Sov. Phys. Solid State 10, 1595 (1969)].

[19]K. R. Lea, M. J. Leask, and W. P. Wolf, J. Phys. Chem. Solids 23, 1381 (1962).

[20]W. R. Hosler (private communication).

[21]P. J. Weller, Electrochem. Soc. 114, 609 (1967); V. J. Abbruscato, E. Banks, and B. R. McGarvey, J. Chem. Phys. 49, 903 (1968).

[22]E. A. Bailey and G. K. Rollefson, J. Chem. Phys. 21, 1315 (1953).

[23]J. N. Demos and G. A. Crosby, J. Phys. Chem. 75, 991 (1971).

[24]P. A. Forrester and S. D. McLaughlan, Phys. Rev. 138, A1682 (1965).

[25]For example S. D. McLaughlan, P. A. Forrester, and A. F. Fray, Phys. Rev. 146, 344 (1966); S. D. McLaughlan, *ibid.* 160, 287 (1967); Ref. 24.

[26]D. R. Bosomworth, Phys. Rev. 157, 709 (1967).

[27]B. G. Wybourne, *Spectroscopic Properties of Rare Earths* (Interscience, New York, 1965), p. 167.

[28]G. M. Zverev, L. S. Kornienko, A. N. Prokhorov, and A. I. Smirnov, Fiz. Tverd. Tela 4, 392 (1962) [Sov. Phys. Solid State 4, 284 (1962)].

[29]Throughout this discussion we have used labeling characteristics of O_h symmetry; realizing, for example, that in C_{2v} symmetry a Γ_7 state becomes Γ_5. Refer to G. F. Koster, J. O. Dimmock, R. G. Wheeler, and H. Statz, *Properties of the Thirty-Two Point Group* (MIT Press, Cambridge, Mass., 1963), p. 104.

[30]H. R. Lewis and E. S. Sabisky, Phys. Rev. 130, 1370 (1963).

[31]M. R. Brown, in *Advances in Quantum Electronics*, edited by D. W. Goodwin (Academic, London, 1970), Vol. I, p. 45.

[32]L. A. Riseberg and H. W. Moos, Phys. Rev. 174, 429 (1968).

[33]P. Denham, G. R. Field, P. L. R. Morse, and G. R. Wilkinson, Proc. Roy. Soc. (London) A317, 55 (1970).